Journal of Colloid and Interface Science 369 (2012) 123–128

Contents lists available at SciVerse ScienceDirect

Journal of Colloid and Interface Science

www.elsevier.com/locate/jcis

Facile controlled synthesis and growth mechanisms of flower-like and tubular MnO_2 nanostructures by microwave-assisted hydrothermal method

Yongliang Li, Jiajun Wang, Yong Zhang, Mohammad Norouzi Banis, Jian Liu, Dongsheng Geng, Ruying Li, Xueliang Sun *

Department of Mechanical and Materials Engineering, University of Western Ontario, 1151 Richmond Street N., London, Ontario, Canada N6A 5B9

ARTICLE INFO

Article history:
Received 18 September 2011
Accepted 5 December 2011
Available online 13 December 2011

Keywords:
Flower-like spheres
Nanotubes
Dissolution–crystallization
Oriented attachment

ABSTRACT

Birnessite flower-like and α-type tubular MnO_2 nanostructures were selectively synthesized through simple decomposition of $KMnO_4$ under hydrochloric acid condition by controlling reaction temperature using a microwave-assisted hydrothermal method. The as-prepared samples were characterized in detail by various techniques including X-ray diffraction, field emission scanning electron microscopy, transmission electron microscopy, high-resolution transmission electron microscopy, Fourier transform-infrared spectroscopy, and Raman scattering spectroscopy. While the growth of flower-like birnessite-MnO_2 might follow a widely accepted Ostwald ripening process, we proposed a formation mechanism of the nanotubular α-MnO_2 based on our evidence, which was assembly of nanorods through an "oriented attachment" process.

1. Introduction

Synthesis of nanostructured materials with controlled shape, architecture, and size is of importance to ensure their property performance in various device applications, such as optics, magnetism, mechanics, and electronics [1]. Among various synthesis approaches, solution-based wet chemical methods feature the virtue of multiplex routes, and high output, templates, surfactants, and complexing species have been applied to control size and structure of the products [2–4]. However, these methods usually imply complex and costly procedures, which are not versatile or environmental friendly.

Recently, microwave irradiation has been increasingly applied to replace conventional heating methods in material synthesis and sample digestion since it provides a selective, fast, and homogenous heat that significantly reduces processing time and cost [5–7]. Combining the microwave irradiation with wet chemical methods such as hydrothermal or solvothermal techniques required temperature and pressure for nanostructure growth can be rapidly achieved, which leads to enhanced kinetics of crystallization and promotes the formation of new phase of product [8]. In this case, nanomaterials with novel structures and architectures are expected to be generated. Up to now, different kinds of nanomaterials have been synthesized via a microwave-assisted route, including NiO [9], ZnO [10], Fe_3O_4 [11], WO_3 [12], Co_3O_4 [13].

Manganese dioxide (MnO_2) nanostructures exhibit distinctive physical and chemical properties and have wide applications in molecular/ion sieves [14], catalysts [15], sensors [16], and energy storage [17]. It is known that the properties of nanostructured MnO_2 highly depend on the crystal structure, dimension, and morphology [18]. Various MnO_2 nanostructures such as nanoparticles [19], nanorods/nanofibers [20], nanowires [21], and nanotubes [22] have been prepared by sol–gel [23], precipitation [24], reflux [25], thermal deposition [26], and hydrothermal [27] techniques. As a direct and one-step wet chemical route, hydrothermal method has been prevalently employed in synthesizing MnO_2 nanostructures. For example, Wang et al. reported a selected-control low-temperature hydrothermal method of synthesizing 1D MnO_2 nanostructures through the oxidation of Mn^{2+} by $S_2O_8^{2-}$, MnO_4^- or ClO^- [28,29]. Cheng et al. synthesized 2D hexagram-like and dendrite-like hierarchical MnO_2 nanostructures by decomposition of $Mn(NO_3)_2$ solution with or without nitric acid [17]. Yu et al. obtained 3D urchin shaped and clewlike MnO_2 nanostructures in the presence of Al^{3+} or Fe^{3+} under hydrothermal condition [30]. However, these conventional hydrothermal methods require prolonged reaction time for more than 12 h, even for several days. Recently, microwave-assisted hydrothermal method (MA-HM) was employed to synthesize octahedral molecular sieves (OMS-2) nanomaterials, and the samples possess better catalytic activity for cinnamyl alcohol oxidation than their conventional counterparts [31]. But to the best of our knowledge, synthesis of MnO_2 nanotubes by MA-HM has not been reported previously.

Herein, we demonstrate a facile rapid procedure to fabricate MnO_2 nanostructures through the decomposition of $KMnO_4$ under

* Corresponding author. Fax: +1 519 6613020.
E-mail address: xsun@eng.uwo.ca (X. Sun).

0021-9797/$ - see front matter © 2011 Elsevier Inc. All rights reserved.
doi:10.1016/j.jcis.2011.12.013

hydrochloric acid condition by MA-HM. 3D hierarchical nanostructures and 1D nanotubes of MnO_2 with different crystallographic forms were selectively obtained by controlling the reaction parameters. The growth mechanism was studied and discussed in detail based on detailed observations in different growth stages. This synthetic route requires no templates, catalysts, or organic reagents, which promises large-scale production of nanostructured MnO_2 with controlled structure and size.

2. Experimental procedure

All the chemicals used in this experiment were of analytical grade from Sigma–Aldrich Company and used without further purification. In a typical synthesis, 1.5 mmol of $KMnO_4$ was added to 20 ml deionized water to form a homogeneous solution. 0.5 ml of HCl (37 wt.%) was then added dropwise into the solution under magnetic stirring. After stirring for 20 min, the obtained solution was transferred to a 100 ml Teflon-lined ceramic-walled vessel. The autoclave was sealed and heated to different reaction temperatures (100, 140, and 180 °C) with the same holding time of 25 min in an Anton Paar Synthos 3000 microwave synthesis system. After the autoclave was cooled down to room temperature, the sample was collected by centrifugation and washed with deionized water and absolute ethanol several times to remove the impurities, and dried in air at 80 °C for 12 h.

The powder X-ray diffraction (XRD) patterns were recorded by a Inel multipurpose diffractometer (MPD) system with Cu Kα radiation (λ = 1.54060 Å) operated at 30 kV and 20 mA. The morphology of the synthesized samples was determined by a Hitachi S-4800 field emission scanning electron microscope (FESEM) operated at 5 kV. Transmission electron microscopy (TEM) images were taken by a Philips CM 10 microscope operated at 80 kV. High-resolution transmission electron microscopy (HRTEM) and selected area electron diffraction (SAED) were characterized by a JEOL 2010 FEG microscope operated at 200 kV. Fourier transform-infrared (FT-IR) measurements were carried out by the KBr method using a Nicolet 6700 FT-IR spectrometer. FT-IR spectra were recorded in the transmittance mode over the range of 400–4000 cm^{-1} by averaging 16 scans at a resolution of 4 cm^{-1}. Raman scattering (RS) spectra were collected on a HORIBA Scientific LabRAM HR Raman spectrometer system equipped with a 532 nm laser. A laser energy filter value of 2 was applied, which prevents decomposition of the samples. The spectra were taken between 100 and 1000 cm^{-1} in a backscattering configuration at room temperature.

3. Results and discussion

3.1. Structure and morphology characterization

The phase purity and crystal structure of MnO_2 were examined by XRD. Different crystal structures can be achieved by controlling the reaction temperatures. As shown in Fig. 1a, all the diffraction peaks of the XRD pattern for the sample prepared at 100 °C can be indexed to the birnessite-type MnO_2 (JCPDS No. 80-1098), which has a lamellar structure and the interlayer distance of MnO_6 octahedra layers is 0.73 nm. The broaden peaks with low intensity observed in XRD pattern suggest that the sample is in poor crystalline state with a short-range crystal form. In particular, the relative intensities of the (001) planes are lower than those in the standard JCPDS data, which suggests that the layers of MnO_6 octahedra are not perfectly oriented [32]. In contrast, the sample prepared at 140 °C (Fig. 1b) can be attributed to the tetragonal phase α-MnO_2 (JCPDS No. 44-0141), and the XRD pattern with sharp and intense peaks indicates a good crystallinity for the α-MnO_2.

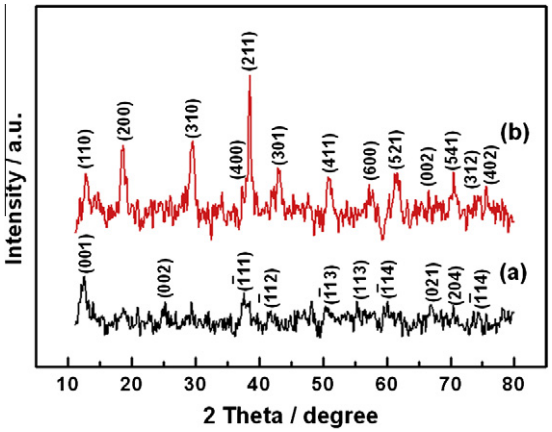

Fig. 1. XRD patterns of the products prepared at (a) 100 °C and (b) 140 °C in 25 min.

MnO_2 with different crystal structures exhibited significantly different morphologies. Fig. 2 shows the SEM images of birnessite-type and α-MnO_2. As shown in Fig. 2a, the birnessite-type MnO_2 sample is composed of uniform flower-like microsphere nanostructures with a diameter of 200–400 nm. The high-magnification images reveal that the microsphere consists of crumpled nanosheets about 10 nm in thickness (Fig. 2b). By comparison, the α-MnO_2 shows typical fibrous shape nanostructures with a length of 2–6 μm (Fig. 2c). The images at higher magnification (Fig. 2d) reveal that they have tubular structures and the diameter is about 100 nm.

The interior structure of the flower-like microsphere nanostructures was further characterized by TEM and HRTEM. Fig. 3a shows core-corona architecture of the birnessite-type MnO_2, which is similar to the previous report [33]. From the TEM image, it can be seen clearly that the nanosheets in the corona are grown perpendicularly/parallel from the core. The selected area electron diffraction (SAED) pattern (inset in Fig. 3a) of a typical microsphere indicates that it is polycrystalline. The HRTEM image (Fig. 3b) indicates that the corona is composed of thin sheets crystallized in the birnessite structure with a *d*-spacing about 0.6 nm. The distance is lower than the *d*-spacing between the (001) planes (0.73 nm), which is due to the dehydrating under the electron beam. It is noticed that the distance between nanosheets is not even and there are some dislocations along the nanosheet direction (red[1] dash circle in Fig. 3b), indicating the poor orientation of the (001) planes, which agrees with the XRD result.

Fig. 3c and d show the TEM and HRTEM images of the α-MnO_2 nanotube structures. As shown in Fig. 3c, the α-MnO_2 nanotubes have relatively uniform outer diameters ranging between 80 and 100 nm, and the wall thickness is about 20 nm. The SAED pattern (inset in Fig. 3c) reveals the single-crystalline nature of the α-MnO_2 nanotubes. The lattice fringes in Fig. 3d show that the interplanar distance perpendicularly to the rod axis is 0.29 nm, which agrees with the *d* value of (001) planes of α-MnO_2. Therefore, the nanotubes grow along the [001] direction. The TEM and HRTEM results are consistent with XRD data, confirming the mono-phase and good crystallinity of the α-MnO_2 nanotubes.

Fourier transform-infrared (FT-IR) and Raman scattering (RS) spectroscopy have been proved to be useful alternatives and/or supplements to X-ray diffraction for structural characterizations of materials [34]. Because they are sensitive to crystalline disorders as well as different local structural properties, FT-IR and RS

[1] For interpretation of color in Figs. 1, 4–6, the reader is referred to the web version of this article.

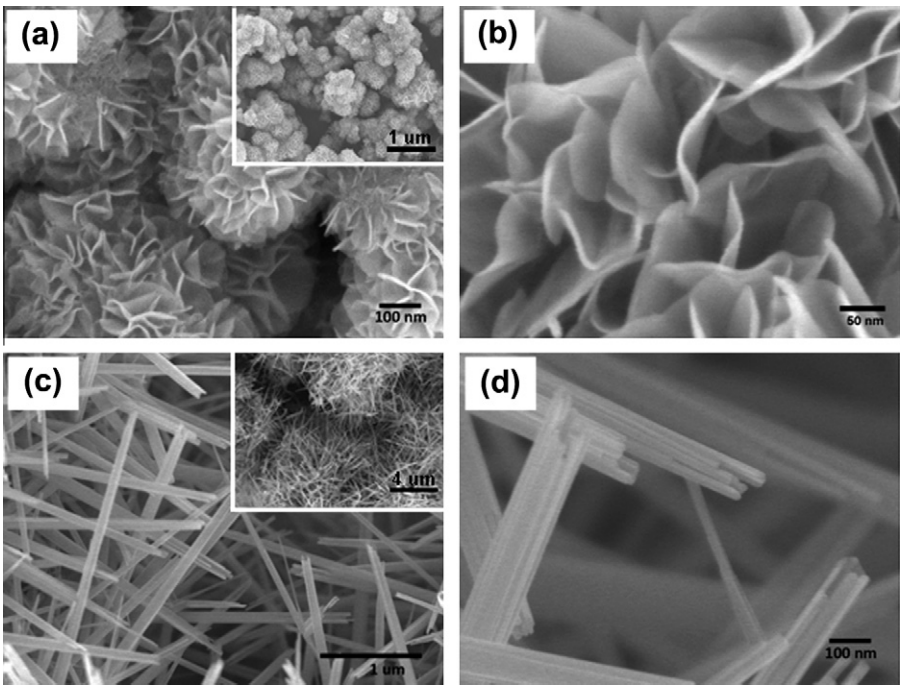

Fig. 2. SEM images of the products prepared at (a and b) 100 °C and (c and d) 140 °C in 25 min. The insets of a and c are the lower magnification images.

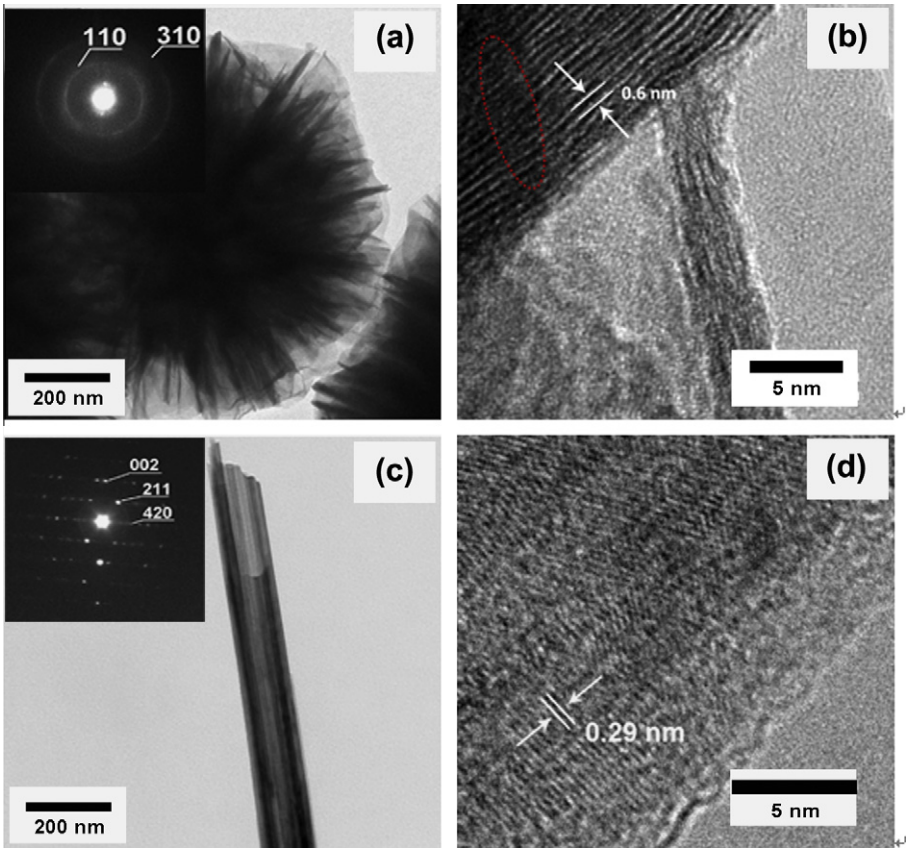

Fig. 3. TEM (a and c) and HRTEM (b and d) images of the products prepared at (a and b) 100 °C and (c and d) 140 °C in 25 min. The insets of a and c show the corresponding SAED patterns.

spectroscopy can yield more complete and reliable description of materials, and further confirm our samples.

The FT-IR spectra of the samples are shown in Fig. 4A. From the spectra results of as-prepared samples, it can be observed that a broadband appears at around 3442 cm^{-1} for both samples, which is caused by the absorbent of interlayer hydrates and some hydroxyl groups not from hydrates but those directly bound to the interlayer metal ions. And the bands at 1635 and 1385 cm^{-1} represent

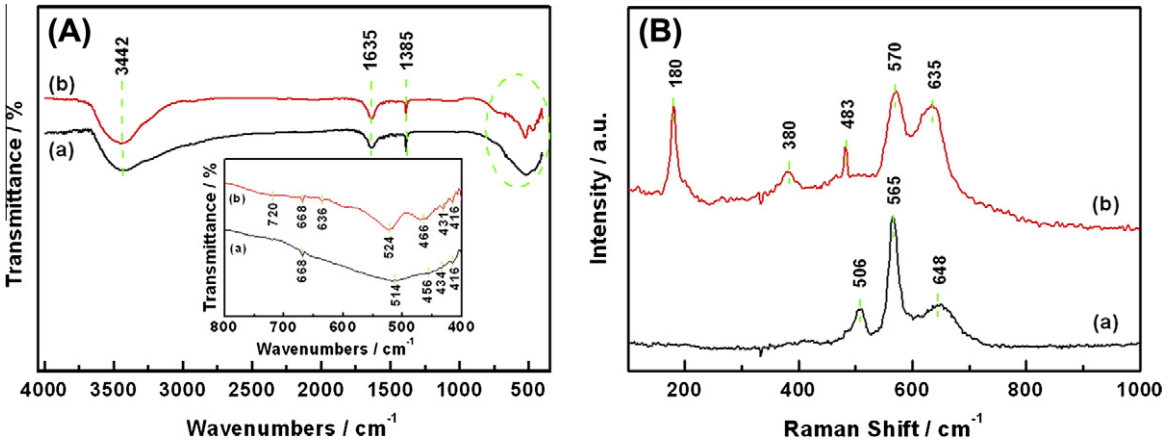

Fig. 4. FT-IR spectra (A) and Raman scattering spectra (B) of the products prepared at (a) 100 °C and (b) 140 °C in 25 min.

the vibration due to the interaction of Mn with surrounding species, such as OH, O, H^+, and K^+. The water molecules or cations intercalated into the MnO_2 interlayer or tunnels were introduced during the synthesis to build/maintain the structures [35]. It has been reported that in hydrous MnO_2 samples, the peaks appear at 1620 and 1280 cm^{-1} [36]. The high frequency shift in our case reveals the strongly bonded nature [37]. The FT-IR spectra results in the region of 800–400 cm^{-1} reveal information about MnO_6 octahedra (inset in Fig. 4A). A major difference between the two kinds of samples has been witnessed in this region. For birnessite-type MnO_2, a broadband is present at 514 cm^{-1} while four weak bands are recorded at 668, 456, 434 and 416 cm^{-1}, respectively. The results are different from that of literatures, viz. the band at 635, 583, 513, 477, and 423 cm^{-1}, respectively [38]. Especially, the band at 423 cm^{-1} indicates the crystalline order of the birnessite compound [34]. The distortion of MnO_6 octahedra is due to the constitutional water in the sample [37]. Obvious differences can be observed for α-MnO_2. Two dominant bands at 524 and 466 cm^{-1} and five weak bands at 720, 668, 636, 431, and 416 cm^{-1} are recorded, which are similar to those previously reported for α-MnO_2 materials [39].

Fig. 4B shows the Raman spectra of birnessite-type and α-MnO_2. Three main contributions at 506, 565, and 648 cm^{-1} are detected for the birnessite-type MnO_2. The Raman band at 648 cm^{-1} can be viewed as the symmetric v_2(Mn–O) stretching vibration of MnO_6 groups, and the band at 565 cm^{-1} is attributed to the v_3(Mn–O) stretching vibration in the basal plane of MnO_6 sheets [40]. The v_3(Mn–O) stretching frequency presents a shift of 10 cm^{-1} toward the low-frequency side, which is attributed to the defect chemistry and the local disorder of the as-prepared birnessite structure [34]. The Raman spectrum of α-MnO_2 nanotubes has several contributions at 180, 380, 483, 570, and 635 cm^{-1}. The low-frequency Raman band at 180 cm^{-1} is assigned to an external vibration that due to the translational motion of the MnO_6 octahedra, while the Raman band at 380 cm^{-1} is caused by the Mn–O bending vibrations. It is emphasized that the relative intensities of two high-frequency Raman bands at 570 and 635 cm^{-1} are correlated to the nature of the tunnel species [39]. Hence, the spectrum reflects the good crystallinity of the α-MnO_2, which is in agreement with the structural studies reported above.

3.2. Growth mechanisms of MnO_2 nanostructures

The formation mechanism of the flower-like MnO_2 microspheres has been widely accepted in the previous report for hydrothermal method [41]. We believe that the microwave-assisted hydrothermal method has a similar mechanism. In brief, firstly, large amount of nuclei form rapidly in a short time and then self-assembly to form amorphous spheres. During the hydrothermal process, an Ostwald ripening process is carried out, in which smaller particles dissolve while the bigger ones grow into sheet-like particles with a lamellar structure. Finally, the sheet-like particles tend to curl and assembly to form a core-corona hierarchical structure.

By contrast, several models have been suggested in terms of the formation of metal or metal oxide nanotubes in a solution-based process. Ye et al. proposed a curving followed by seaming of molecular layers mechanism for the tube-formation process of materials with layered structure [42]. Mo et al. suggested a template-roll-growth and template-twist-join-growth mechanism for the formation of Te nanotubes [43]. Wang and Li proposed a rolling mechanism for the conversion from MnO_2 nanosheets to nanotubes [28]. Luo et al. proposed a tip-/end-etching process for the formation of MnO_2 nanotubes [44]. However, no evidence is shown to support these hypotheses in our system.

The reaction in our process could be described as follows:

Half reaction:

$$2Cl^- \rightarrow Cl_2 + 2e^- \qquad (E^0 = -1.3595\ V)$$

$$MnO_4^- + 4H^+ + 3e^- \rightarrow MnO_2 + 2H_2O \quad (E^0 = +1.695\ V)$$

Overall reaction:

$$2MnO_4^- + 8H^+ + 6Cl^- \Longleftrightarrow 2MnO_2 + 3Cl_2 + 4H_2O$$

To understand the formation of the α-MnO_2 nanotubes, the reaction under different periods of time was investigated. Fig. 5 shows the TEM images of three samples taken at different stages of the reaction. When the reaction proceeded for 5 min, some microspheres with core-corona architecture were produced with a diameter about 1 μm, and the thickness of nanosheets is about 10 nm (Fig. 5a). After 10 min, the microspheres tended to collapse and some fibrous structures formed. From Fig. 5b, it can be seen that three different types of fibrous structures formed: nanorod with a diameter about 20 nm (Fig. 5d); bundle-like tube with a diameter about 50 nm (Fig. 5e); and nanotube with a diameter about 80 nm (Fig. 5f). As shown in Fig. 5e, the bundle-like tube consists of nanorods about 16 nm in diameter, which is consistent to the diameter of the single nanorod in Fig. 5d. Fig. 5f shows that the nanotube has smooth surface but an uneven end, and the wall

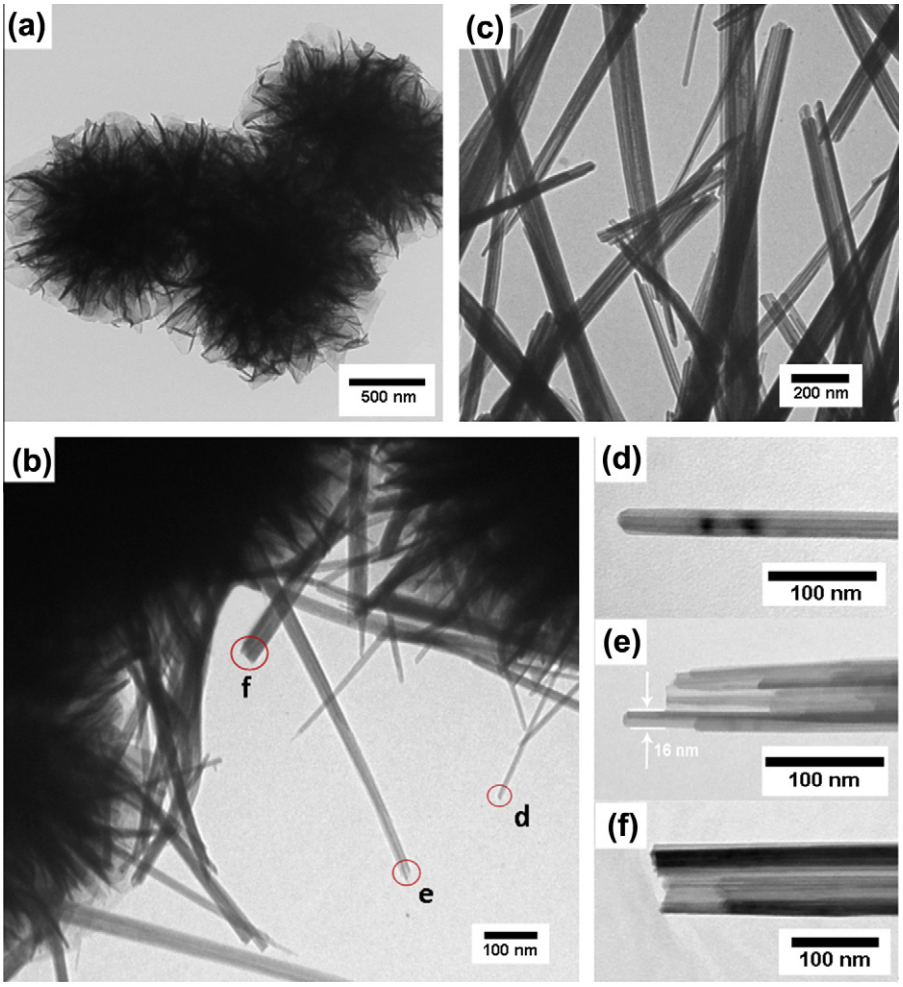

Fig. 5. TEM images of the products prepared in 5 min (a), 15 min (b, d, e, and f), and 25 min (c) at a reaction temperature of 140 °C.

thickness is about 20 nm. When the reaction time was prolonged to 25 min, the nanotubes with a diameter of 80–100 nm formed in majority (>85%) (Fig. 5c).

It has been reported that α-MnO_2 nanowires/nanorods tended to assemble along lateral surface and form thick nanorods through an "oriented attachment" mechanism under the hydrothermal condition since the formation of bundles could reduce the surface-to-volume ratio and the surface energy [45–48]. The exact mechanism for the formation of tubular nanostructures in our case is still under investigation. But we believe that two mechanisms, as shown in Fig. 6, are responsible for the formation of the nanotubes: (a) a dissolution–crystallization process that converts less ordered precursors into nanorods (from nanosheets to nanorods); (b) an "oriented attachment" process that aggregates nanorods along the lateral faces to form tubular products. The formation process of the MnO_2 nanotubes can be described as follows: At the initial stage, the 3D hierarchical architectures formed as described above; then, nanorods were produced because at higher temperatures (140 °C) thermal energy is enough to overcome the activation energy required for the conversion from nanosheets to nanorods [49]. Meanwhile, some nanorods tended to assemble along their side surfaces to reduce the surface energy. The small gaps between nanorods were filled rapidly due to coarsening during aging, which led to reconstruction of boundaries and smoothing of the surfaces. That is the reason why the nanotubes show a single-crystalline nature. Since the growth along the length direction ([001] direction) was very fast that the mass transport to the growing regions would lead to under-

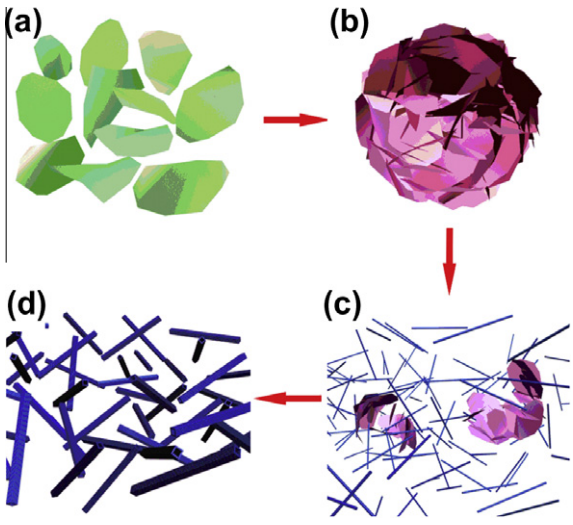

Fig. 6. Schematic illustration of the formation stages of different shapes of the MnO_2 nanostructures.

saturation of reaction species in the central portions of the growing faces, {001} planes, and eventually resulted in the formation of tubular structure having hollow interiors. Similar process has been observed in the formation of Te nanotubes [50]. It is necessary to

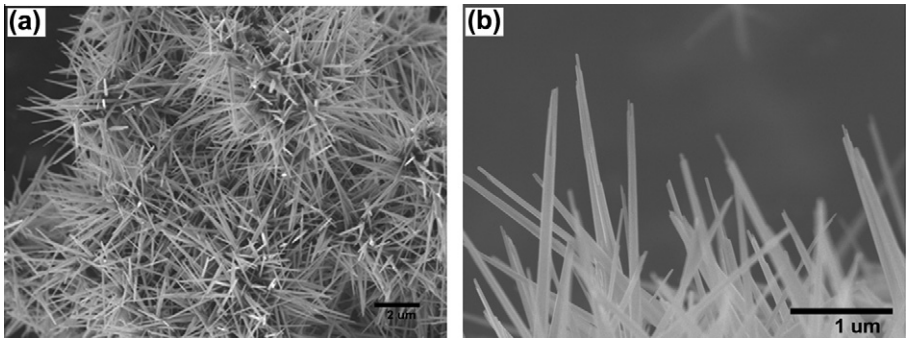

Fig. 7. SEM images of the product prepared at 180 °C in 25 min.

note that the dissolution–crystallization and "oriented attachment" are two simultaneous processes in the crystal growth [51], the separated stages in Fig. 6c and d are illustrated just for the convenience of explanation. In our experiments, it was found that morphology of the product prepared at 180 °C was different from that prepared at 140 °C, showing a hollow needle-like structure, which was due to the fast growth rate of the nanorods at the external wall of the nanotubes (Fig. 7). This further confirms the proposed growth mechanism.

4. Conclusions

In summary, we report a facile microwave-assisted hydrothermal route for the synthesis of 3D hierarchical and 1D tubular MnO_2 nanostructures. The crystal phase and morphology can be easily tailed by adjusting reaction temperature. The formation of MnO_2 nanotubes follows the dissolution–crystallization and "oriented attachment" process. Compared to conventional heating methods, the microwave-assisted hydrothermal approach features rapid growth of nanostructured MnO_2 with controlled structure, which is ideal for large-scale production. We believe that this study not only provides a new growth scheme of MnO_2 nanotube formation but also gives a rational strategy in synthesis and design of nanomaterials with complex architecture and novel properties.

Acknowledgments

This research was supported by Natural Sciences and Engineering Research Council of Canada, Canada Research Chair Program, Canada Foundation for Innovation, Ontario Early Researcher Award and the University of Western Ontario. The authors would like to appreciate Mr. Fred Pearson at McMaster University for the fruitful discussion.

References

[1] Z. Li, Y. Ding, Y. Xiong, Y. Xie, Cryst. Growth Des. 5 (2005) 1953.
[2] G. Ji, S. Tang, B. Xu, B. Gu, Y. Du, Chem. Phys. Lett. 379 (2003) 484.
[3] S. Chou, C. Zhu, S. Neeleshwar, C. Chen, Y. Chen, C. Chen, Chem. Mater. 21 (2009) 4955.
[4] T. Almeida, M. Fay, Y. Zhu, P. Brown, J. Phys. Chem. C 113 (2009) 18689.
[5] J. Menéndez, A. Domínguez, M. Inguanzo, J. Pis, J. Anal. Appl. Pyrol. 71 (2004) 657.
[6] J. Liu, K. Li, H. Wang, M. Zhu, H. Yan, Chem. Phys. Lett. 396 (2004) 429.
[7] M. Nüchter, B. Ondruschka, W. Bonrath, A. Gum, Green. Chem. 6 (2004) 128.
[8] S.D. Naik, T.C. Jagadale, S.K. Apte, R.S. Sonawane, M.V. Kulkarni, S.I. Patil, S.B. Ogale, B.B. Kale, Chem. Phys. Lett. 452 (2008) 301.
[9] T. Lai, Y. Lai, J. Yu, Y. Shu, C. Wang, Mater. Res. Bull. 44 (2009) 2040.
[10] A. Phuruangrat, T. Thongtem, S. Thongtem, Mater. Lett. 63 (2009) 1224.
[11] H. Zhou, R. Yi, J. Li, Y. Su, X. Liu, Solid State Sci. 12 (2010) 99.
[12] Y. Ma, L. Zhang, X. Cao, X. Chen, Z. Xue, Cryst. Eng. Commun. 12 (2010) 1153.
[13] W. Li, Mater. Lett. 62 (2008) 4149.
[14] L. Wang, C. Meng, M. Han, W. Ma, J. Colloid Interface Sci. 325 (2008) 31.
[15] R. Kumar, S. Sithambaram, S. Suib, J. Catal. 262 (2009) 304.
[16] A. Lima, N. Bocchi, H. Gomes, M. Teixeira, Sensors 9 (2009) 6613.
[17] F. Cheng, J. Zhao, W. Song, C. Li, H. Ma, J. Chen, P. Shen, Inorg. Chem. 45 (2006) 2038.
[18] S. Devaraj, N. Munichandraiah, J. Phys. Chem. C 112 (2008) 4406.
[19] D. Zheng, Z. Yin, W. Zhang, X. Tan, S. Sun, Cryst. Growth Des. 8 (2006) 1733.
[20] G. Xi, Y. Peng, Y. Zhu, L. Xu, W. Zhang, W. Yu, Y. Qian, Mater. Res. Bull. 39 (2004) 1641.
[21] S. Zhu, H. Zhou, M. Hibino, I. Honma, M. Ichihara, Adv. Funct. Mater. 15 (2005) 381.
[22] D. Zheng, S. Sun, W. Fan, H. Yu, C. Fan, G. Cao, Z. Yin, X. Song, J. Phys. Chem. B 109 (2005) 16439.
[23] J. Liu, Y. Son, J. Cai, X. Shen, S. Suib, M. Aindow, Chem. Mater. 16 (2004) 276.
[24] V. Subramanian, H. Zhu, B. Wei, Chem. Phys. Lett. 453 (2008) 242.
[25] X. Liu, S. Fu, C. Huang, Powder Technol. 154 (2005) 120.
[26] S. Kim, S. Kim, S. Oh, Chem. Mater. 11 (1999) 557.
[27] R. Chen, P. Zavalij, M. Whittingham, Chem. Mater. 8 (1996) 1275.
[28] X. Wang, Y. Li, Chem. Eur. J. 9 (2003) 300.
[29] Y. Li, X. Li, R. He, J. Zhu, Z. Deng, J. Am. Chem. Soc. 124 (2002) 1411.
[30] P. Yu, X. Zhang, D. Wang, L. Wang, Y. Ma, Cryst. Growth Des. 9 (2009) 528.
[31] H. Huang, S. Sithambaram, C. Chen, C. Kithongo, L. Xu, A. Iyer, H. Garces, S. Suib, Chem. Mater. 22 (2010) 3664.
[32] D. Portehault, S. Cassaignon, E. Baudrin, J.-P. Jolivet, J. Mater. Chem. 19 (2009) 2407.
[33] D. Portehault, S. Cassaignon, N. Nassif, E. Baudrin, J.-P. Jolivet, Adv. Mater. 47 (2008) 6441.
[34] C. Julien, M. Massot, C. Poinsignon, Spectrochim. Acta Part A 60 (2004) 689.
[35] W. Xiao, D. Wang, X. Lou, J. Phys. Chem. C 114 (2010) 1694.
[36] J. Fernandes, B. Desai, D. Kamat, Electrochim. Acta 28 (1983) 309.
[37] M. Ananth, S. Pethkar, K. Dakshinamurthi, J. Power Sour. 75 (1998) 278.
[38] L. Kang, M. Zhang, Z. Liu, K. Ooi, Spectrochim. Acta Part A 67 (2007) 864.
[39] T. Gao, H. Fjellvåg, P. Norby, Anal. Chim. Acta 648 (2009) 235.
[40] C. Julien, M. Massot, R. Baddour-Hadjean, S. Franger, S. Bach, J. Pereira-Ramos, Solid State Ionics 159 (2003) 345.
[41] N. Xu, Z. Liu, X. Ma, S. Qiao, J. Yuan, J Nanopart. Res. 11 (2009) 1107.
[42] C. Ye, G. Meng, Z. Jiang, Y. Wang, G. Wang, L. Zhang, J. Am. Chem. Soc. 124 (2002) 15180.
[43] M. Mo, J. Zeng, X. Liu, W. Yu, S. Zhang, Y. Qian, Adv. Mater. 14 (2002) 1658.
[44] J. Luo, H. Zhu, H. Fan, J. Liang, H. Shi, G. Rao, J. Li, Z. Du, Z. Shen, J. Phys. Chem. C 112 (2008) 12594.
[45] S. Chen, J. Zhu, Q. Han, Z. Zheng, Y. Yang, X. Wang, Cryst. Growth Des. 9 (2009) 4356.
[46] D. Portehault, S. Cassaignon, E. Baudrin, J.-P. Jolivet, Chem. Mater. 19 (2007) 5410.
[47] T. Gao, M. Glerup, F. Krumeich, R. Nesper, H. Fjellvåg, P. Norby, J. Phys. Chem. C 112 (2008) 13134.
[48] X. Zhang, W. Yang, J. Yang, D. Evans, J. Cryst. Growth 310 (2008) 716.
[49] D. Walanda, G. Laurance, S. Donne, J. Power Sour. 139 (2005) 325.
[50] B. Mayers, Y. Xia, Adv. Mater. 14 (2002) 279.
[51] Y. Li, H. Tan, O. Lebedev, J. Verbeeck, E. Biermans, G. Tendeloo, B. Su, Cryst. Growth Des. 10 (2010) 2969.